Title

Improvement and analysis of the hydrogen-cerium redox flow cell

Authors

Tucker, Michael C

Weiss, Alexandra

Weber, Adam Z

Publication Date

2016-09-01

DOI

10.1016/j.jpowsour.2016.07.105

Improvement and Analysis of the Hydrogen-Cerium Redox Flow Cell

Michael C. Tucker*, Alexandra Weiss, and Adam Z. Weber

Energy Conversion Group, Energy Technologies Area

Lawrence Berkeley National Laboratory

1 Cyclotron Rd

Berkeley, CA 94720 USA

Abstract

The H_2-Ce redox flow cell is optimized using commercially-available cell materials. Cell performance is found to be sensitive to the upper charge cutoff voltage, membrane boiling pretreatment, methanesulfonic-acid concentration, (+) electrode surface area and flow pattern, and operating temperature. Performance is relatively insensitive to membrane thickness, Cerium concentration, and all features of the (−) electrode including hydrogen flow. Cell performance appears to be limited by mass transport and kinetics in the cerium (+) electrode. Maximum discharge power of 895 mW cm^{-2} was observed at 60°C; an energy efficiency of 90% was achieved at 50°C. The H_2-Ce cell is promising for energy storage assuming one can optimize Ce reaction kinetics and electrolyte.

*mctucker@lbl.gov

Phone 1-510-486-5304

Fax 1-510-486-4260

LBNL; 1 Cyclotron Rd; MS 70-108B; Berkeley CA 94720; USA

1. Introduction

Redox flow batteries (RFB) with various solution chemistries are being developed for large-scale energy storage [1-5]. Advances in redox-active species, electrocatalysts, and separators are required to meet the stringent cost and durability requirements for affordable storage, and recent years have seen many new contributions to the field, which also highlight the necessary areas for improvement [2]. One promising class of RFB utilizes hydrogen gas as the negative working fluid, and an aqueous solution of redox-active species as the positive working fluid. Hydrogen is inexpensive, can be electrochemically compressed to minimize storage volume, and has excellent reaction kinetics. Liquid that crosses through the membrane from the (+) to (–) side is easily separated from the hydrogen gas for return to the positive-electrode tank, simplifying electrolyte balancing. With only one side of the cell containing liquid, pumping and shunt-current losses are expected to be minimized. Furthermore, the adoption of cell architecture derived from mature high-power proton-exchange-membrane (PEM) fuel cells provides excellent cell performance metrics.

Various RFBs with hydrogen (–) electrode have been reported. Hydrogen-halogen cells using primarily Cl_2 and Br_2 have been reviewed recently, and provide among the highest reported power and efficiency metrics for RFBs due to fast, reversible kinetics and moderate self-discharge [6,7]. For example, 1.4 W cm^{-2} discharge power density, 90% peak energy efficiency, and 80% energy efficiency at 0.4 A cm^{-2} were achieved at room temperature for the H_2-Br_2 system, which has an open circuit voltage (OCV) of 1.09 V [8,9]. The H_2-Fe cell provides the potential for extremely inexpensive and benign iron-based electrolyte, however at a rather low cell potential (0.77V) [10-12]. Optimization of this cell, including addition of supporting electrolyte, achieved peak power density of 250 mW cm^{-2} and energy storage efficiency of 78% [10]. Cost analysis suggested that although the active materials are very inexpensive, cell performance was too low to be economically attractive given the cost of cell/stack materials. The H_2-V system offers open-circuit potential of 1 to 1.2 V, depending on vanadium concentration. Proof-of-

concept work demonstrated moderate performance (114 mW cm^{-2}) and 60% energy efficiency [13]. The main limitations for this cell are thought to be vanadium diffusion in the (+) electrode and interaction of crossover vanadium with the Pt (–) catalyst [14]. The H_2-Ce system provides unusually high open circuit voltage (1.5 to 1.7 V), which could enable high power and energy densities. A proof-of-concept for this system demonstrated 148 mW cm^{-2} peak discharge power and 88% energy efficiency, and suggested that cerium kinetics limits cell performance [15]. The Ce (+) electrode operates at potentials outside the stability window of water; however, extensive work on the aqueous Zn-Ce RFB indicates that appropriate solution chemistry and operating protocols can mitigate deleterious oxygen evolution [16]. Due to its potential for high energy and high power densities, this cell is explored in this paper to see if a more optimized system is promising.

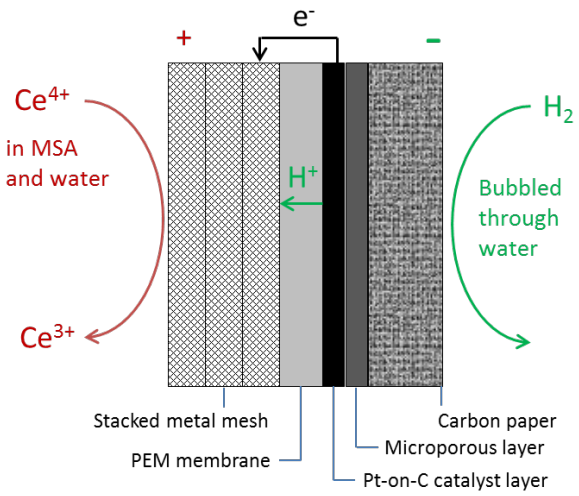

Figure 1. Schematic of H_2-Ce redox flow cell.

The H_2-Ce redox-flow system consists of an electrochemical cell that is fed reactants from storage tanks containing gaseous hydrogen (negative side) and an aqueous solution of Ce^{4+} (positive side), as shown in Figure 1. During discharge, hydrogen is oxidized to protons at the negative electrode. The protons pass through an ion-conducting membrane and balance the reduction of Cerium(IV) methanesulfonate to

Cerium(III) methanesulfonate at the positive electrode, and methanesulfonic acid (MSA) is released into solution from the Cerium(IV) methanesulfonate complex. The electrochemical reactions are shown below with the forward direction corresponding to discharge and the reverse to charge. Note that the potential for Reaction 2 depends on solvent type and concentration [16,17].

Negative: $\frac{1}{2}H_2(g) \rightleftharpoons H^+(aq) + e^-$ $\quad E^0 = 0.00\,V$ (1)

Positive: $Ce^{4+}(aq) + e^- \rightleftharpoons Ce^{3+}(aq)$ $\quad E^0 = 1.5 - 1.75V$ (2)

Overall: $Ce^{4+}(aq) + \frac{1}{2}H_2 \rightleftharpoons Ce^{3+}(aq) + H^+(aq)$ $\quad E^0 = 1.5 - 1.75$ (3)

The promise of the high OCV offered by the H_2-Ce couple is tempered by the relatively low current density reported for aqueous cerium electrochemistry on Pt catalyst in general [16-20], and moderate power density demonstrated for the H_2-Ce cell specifically [15]. In this work, we optimize the cell architecture and materials to achieve significantly improved power density and efficiency with commercially-available materials, and find that future improvements may require development of new cerium electrocatalysts and electrode architectures.

2. Experimental Methods

Cells were assembled and tested using 10 cm^2 Fuel Cell Technologies hardware and equipment discussed in detail elsewhere [8,9,21,22]. A graphite serpentine flow field was used on the negative side (Fuel Cell Technologies). Serpentine or flow-through Niobium flowfields were used on the positive side to avoid carbon oxidation or metal corrosion (Treadstone Technologies, Inc.). The (+) electrode material was Pt woven mesh (Alfa Aesar, 0.17 mm thick, 52 mesh, 0.1 mm diameter wire), Ti woven mesh (Alfa Aesar, 0.22 mm thick, 50 mesh, 0.102 mm diameter wire), platinized titanium expanded mesh (Metakem type G, 4 x 2 mm diamond holes between 0.5 x 0.5 mm strands), platinized niobium expanded mesh (Gold

Plating Services, 3 x 1.5 mm diamond holes between 0.3 x 0.15 mm strands), or nanostructured thin-film (NSTF) platinum catalyst layer (3M Company). The (–) electrode was 0.4 mg/cm^2 Pt/C printed on Sigracet GDL 24BC gas-diffusion layer (GDL), provided by Ion Power. Nafion 212 membranes were used, except where noted. Membranes were pretreated by boiling successively in 3% H_2O_2, DI water, 0.5 M sulfuric acid, and DI water for 1 h each, except where noted. The peroxide boiling step was skipped for NSTF-coated samples. Boiled membranes were assembled into the cell in the hydrated state to maximize conductivity [22], as crossover was found not to be a dominant concern for this system, as discussed in Section 3.2.3. Thickness of the incompressible gaskets around the active cell materials was chosen to achieve 20 to 25% compression of the (–) electrode upon assembly.

Cells were operated with hydrogen bubbled through water (200 ml min^{-1}) and 0.6M cerium methanesulfonate with 3 to 6 M MSA solution (150 ml min^{-1}), except where noted. Solution volume for polarization curves was 300 mL, and for efficiency mapping was 20 mL. Hydrogen pressure was controlled with a backpressure regulator on the cell exhaust line. The (–) hydrogen exhaust was passed through a closed-bottom tube to collect any crossover liquid coming through the membrane from the (+) side; however, typically no liquid was observed, and the (–) electrode was found dry upon cell disassembly. Polarization curves (5 to 30 mA/cm^2 steps of 10 s each), AC impedance (at OCV), and cycling efficiency curves according to a protocol discussed elsewhere [11,21] (typically with voltage limits of 0.2 to 1.9 V), were obtained with a Bio-Logic VMP3 potentiostat. AC impedance was taken by discharging at 120 mA cm^{-2} while scanning from 200 kHz to 10 Hz with 1 mA cm^{-2} perturbation. Before testing, solutions were charged by holding the cell at 2 V until the theoretical charge required for 100% state of charge was achieved (the charging current also dropped significantly at the end of charge). Cerium utilization was determined from coulometry during cell operation. For each current density of interest, the cell was charged and then discharged, and the discharge capacity was used to determine the amount of cerium utilized, which was then compared to the total amount available (calculated from

solution volume and concentration). Elevated-temperature experiments were conducted with cartridge heaters and a thermocouple in the cell hardware, and the solution tank submerged in a heated water bath.

Various cerium salts were screened for use in solution preparation. Solutions were prepared by adding the salt to water, and then slowly adding MSA. Cerium nitrate and cerium sulfate were ruled out based on observation of low solubility. Cerium carbonate was the most favorable, as it dissolved completely and produced a clear solution after off-gassing CO_2 *via* the conversion to cerium methanesulfonate. For 0.6 M Ce solutions, greater than 1 M MSA was required to achieve complete dissolution, and MSA concentrations in the range of 2 to 6 M were tested. For 4 M MSA, a range of cerium concentrations was tested; for 0.2 to 0.6 M Ce, compete solubility was achieved, but for 0.8 and 1 M Ce, precipitation was observed during cell operation. Furthermore, it was found that charging various solutions by holding the cell potential at 2 V until the current dropped to close to zero caused precipitation. Therefore, the typical cycling protocol charged the cell to lower voltage cutoff with no prolonged constant-voltage hold to avoid precipitation (see Section 3.1).

Solution conductivity was assessed with a Symphony 4-probe conductivity cell (VWR Scientific) and Orion Star portable conductivity meter (Thermo Scientific).

3. Results and Discussion

3.1 Cell operation

Aqueous cerium solutions were prepared from Ce^{3+}-carbonate, so the solution was first introduced into the cell in the fully discharged state (0% SOC). Before obtaining cell performance data, the solution was fully charged to roughly 100% SOC (all Ce^{4+}), during which the clear starting solution turned dark yellow. The OCV increases roughly linearly from 1.59 V at 0% SOC to 1.73 V at 100% SOC, as shown in Figure 2a. Clearly, a voltage cutoff limit above 1.73 V is required to achieve complete charging, and limits between 1.8 and 2.0 V were explored, as discussed below.

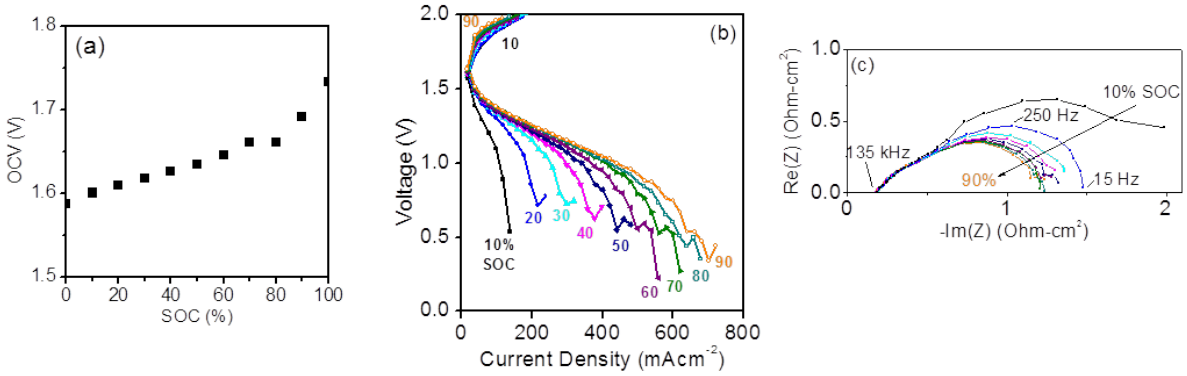

Figure 2. Performance variation with state of charge. (a) Open-circuit voltage and (b) charge and discharge polarization for a stack of 4 Pt meshes as (+) electrode, 0.6 M Ce and 4 M MSA at 65 mL min^{-1}, and boiled NR212 membrane. (c) AC impedance at 120 mA cm^{-2} discharge current for a stack of 8 Pt meshes as (+) electrode, 0.6 M Ce and 5 M MSA at 65 mL min^{-1}, and boiled NR212 membrane.

Cell performance varies significantly with SOC as shown in Figure 2b. Charge performance decreases and discharge performance increases with increasing SOC, following the variation in Ce^{3+} and Ce^{4+} concentrations. The shape and trend of the discharge limiting current suggests significant Ce^{4+} concentration polarization at high current density. The last points near the limiting current are somewhat unstable, as they are at the limiting current and therefore sensitive to peristaltic pulsing in the pumping rate, which was improved for later experiments. Significant activation potential (about 200 mV) is evident in the low-current region, similar to the all-vanadium cell [23], and in contrast to the H_2-Br_2 cell, which exhibits fast kinetics and linear, ohmic-dominated charge and discharge curves [8,24]. Note that the hydrogen concentration at the (−) electrode does not change with variations in SOC as excess hydrogen flows through the cell during operation, suggesting that the activation polarization arises at the (+) electrode. Impedance spectra (Fig. 2c) taken during discharge show a small ohmic impedance and large polarization semicircle, consistent with the previous report on the H_2-Ce system that assigned the large

low-frequency polarization to charge transfer at the cerium electrode [15]. The trend of total impedance with SOC is consistent with the trend of discharge performance, showing increased polarization as Ce^{4+} is consumed (thus increasing kinetic and concentration polarization). The ohmic impedance is only 20% of the value in the previous report, due to the thinner, pretreated membrane used here and discussed below in Section 3.2.3. Even so, the ohmic impedance is about 2 times higher than the membrane resistances seen in the H_2-Br_2, H_2-Fe, and vanadium RFB systems, consistent with a significant deviation of membrane properties in the presence of cerium-MSA solution [10,22,25].

Cell efficiency during constant-current cycling was assessed by adapting protocols discussed elsewhere [11,21], in which galvanostatic full-cycles between fixed voltage cutoffs are used to assess round-trip efficiency. Cycles are repeated at various current densities, with utilization, coulombic efficiency, voltaic efficiency, and energy efficiency determined as a function of current density. A typical charge-discharge cycle is shown in Figure 3a. Both half-cycles show a featureless sloping plateau, consistent with the monotonic OCV and performance dependence on SOC (Figure 2). There is a sharp decrease in voltage at the end of discharge, consistent with nearly complete conversion to Ce^{3+} (0% SOC). In contrast, the end of charge increases in slope, but does not rise rapidly as would be expected in the case of complete conversion to Ce^{4+}. This suggests that the charging process limits utilization (100% SOC is not achieved). Increasing the charge voltage limit was explored as a way to increase utilization, and Figure 3b shows it to be quite sensitive. Increasing to 1.9 V limit significantly increases utilization, especially at higher current density where ohmic and kinetic overpotentials are significant contributors to cell potential and cause the limit to be reached at lower SOC. Near complete utilization (100% SOC) is achieved only for a 2 V limit. For lower voltage limits, self-discharge (discussed below) limits the maximum utilization achieved at low current density. This sensitivity of utilization is important from a system-design perspective, as low utilization drives up the cost of storage capacity (for both cerium and storage-tank expenditures).

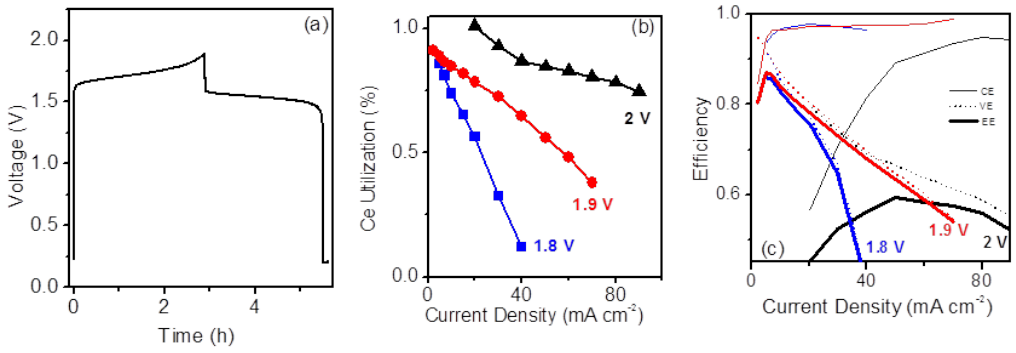

Figure 3. (a) Full charge/discharge cycle at 10 mA cm^{-2} with 1.9 V charge cut-off. Impact of charge cut-off voltage on (b) Ce utilization and (c) efficiency (thin lines – coulombic efficiency, dashed lines – voltage efficiency, thick lines – energy efficiency). Stack of 4 Pt meshes as (+) electrode, 0.6 M Ce and 4 M MSA at 65 mL min^{-1}, and boiled NR212 membrane.

The voltage cutoff limit was also found to be important for energy efficiency, as shown in Figure 3c. The general shape of the energy-efficiency curves is similar to those for H_2-Br_2 and H_2-Fe redox-flow cells [8,11,21,22]; low coulombic efficiency at low current (typically caused by crossover of active species) and low voltage efficiency at high current (caused by cell overpotentials) result in an optimum energy efficiency at an intermediate current density. With a 2 V limit, severely reduced coulombic efficiency causes less than 60% peak energy efficiency to be achieved. We speculate this is due to the oxygen-evolution reaction (OER) at high voltage competing with cerium oxidation; evolved oxygen is released from the system and charge associated with the OER is not recovered during discharge. This is consistent with ex-situ 3-electrode cyclic voltammetry evaluation using a Pt mesh in the cerium-MSA solution, for which rapidly increasing current was observed above 1.8 V vs Ag/AgCl (2.03 V vs SHE) and higher, with bubble formation. In contrast, for 1.8 and 1.9 V limits in that cell, coulombic efficiency above 97% is achieved over a wide range of current density. At very low current density (below 5 mA cm^{-2}), crossover through the membrane and concomitant self-discharge reduces coulombic efficiency, as discussed below

in Section 3.2.3. In all cases, voltage efficiency limits energy efficiency at high current density. A peak energy efficiency of 87% and cerium utilization of 86% are achieved simultaneously with the 1.9 V limit, albeit at a low current density of 7 mA cm^{-2}. Based on the impact on both utilization and efficiency, we selected 1.9 V as the optimum charge voltage limit, and this was used for all further experiments. It is worth noting that the charge voltage limit restricts the maximum charge current density as clearly seen in Figure 3a, so asymmetric charge/discharge current density may be required in a real system. For example, operation might include low-current charge during off-peak times and high-current peak discharge.

3.2 Cell materials and architecture

3.2.1 Cerium (+) electrode

Platinum is a common choice for previous studies of cerium-based flow cells, based on good activity for cerium oxidation and reduction, and stability at high potential (where oxidation of carbon electrodes is a concern) [16]. Previous proof-of-concept work on the H_2-Ce flow cell utilized platinized titanium expanded mesh as the (+) electrode [15]. Here, we explore a variety of mesh types, as shown in Figure 4. Platinized expanded Ti and Nb mesh provide similar, moderate performance. The surface area of the coarse expanded mesh exposed to the cerium electrolyte fluid is relatively low (estimated to be 0.8 cm^2 exposed surface per cm^2 of cell area), and most of the flat face is compressed into the membrane which limits in-plane convection between adjacent holes. We switched to woven Pt mesh composed of fine round wire (1.3 cm^2 per cm^2), which improved performance. Although solid Pt mesh would be too expensive for implementation in a full-scale system, we expect that platinized Ti mesh with similar geometry would provide similar performance at greatly reduced cost. Cost-effective platinum electrodes require high surface area with relatively low loading. The NSTF electrode architecture developed by 3M for fuel cells and electrolyzers provides a thin (< 1 μm), high surface-area electrode of Pt whiskers extending from and partially embedded in the membrane, with roughness factor an order of magnitude higher than for the mesh [26]. Addition of an NSTF electrode layer to a single Pt mesh greatly increases performance, as seen in Figure 4b, confirming that the cell performance is limited by Pt active area.

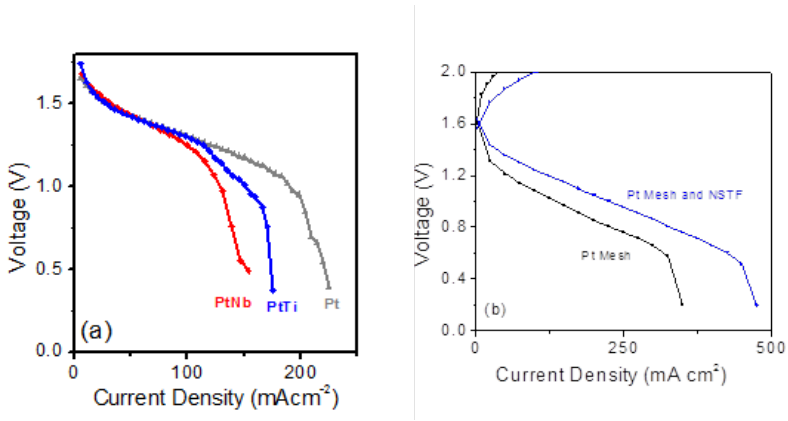

Figure 4. Impact of (+) type on performance. (a) Single woven Pt, expanded platinized Nb, or expanded platinized Ti mesh as (+) electrode, 0.6 M Ce and 4 M MSA at 65 mL min^{-1}, and boiled NR212 membrane. (b) Enhancement of cell performance with addition of NSTF Pt layer on the (+) side of the membrane. Single Pt mesh (with or without NSTF) as (+) electrode, 0.6 M Ce and 5 M MSA at 70 mL min^{-1}, and boiled NR212 membrane.

For all electrodes, there appears to be a mass-transport limit to the current density. As shown in Figure 5, flowrate has a strong impact on the limiting current at low flowrate, and a flowrate above 100 mL min^{-1} is required for the performance to be roughly independent of flowrate. Discharge current of 500 mA cm^{-2} is equivalent to complete reduction of only 5 mL min^{-1} of cerium solution, so bulk depletion of reactant does not cause the limiting current (single-pass utilization varies from 8 to 2.5% at flowrates of 46 and 200 mL min^{-1}, respectively). Rather, sluggish diffusion of cerium-MSA complex to the active Pt surface is expected to give rise to concentration polarization (i.e., diffusion and not convection dominates at low flowrates). The cerium diffusion coefficient at relevant MSA concentrations is reported to be in the range 0.27 to 0.5 10^{-6} cm^2 s^{-1} [17,27], about an order of magnitude lower than the diffusion coefficient of bromine and vanadium ions in redox flow-cell solutions, so significant mass-transport limitation is not surprising [28-30]. Increasing the flowrate forces convection, alleviating mass-transport limitations.

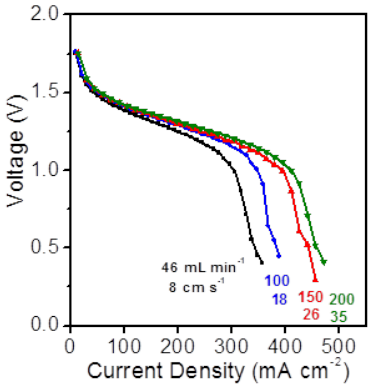

Figure 5. Influence of flowrate on discharge performance. Stack of 4 Pt meshes as (+) flowthrough electrode, 0.6 M Ce and 4 M MSA, and boiled NR212 membrane.

The use of a flow-through electrode is also known to increase transport-limited performance in redox flow cells by forcing convection through the entire bulk of the electrode [24]. A thick electrode is preferred in this geometry to reduce pressure drop. Figure 6 shows performance for a flow-through electrode with various stacks of multiple meshes. Increasing the number of stacked Pt meshes increases performance significantly (i.e from 140 mW cm^{-2} peak power for one mesh to 415 mW cm^{-2} for 8 meshes). As the number of meshes increases, electronic bulk and contact resistances increase, ionic conduction path length in the electrolyte increases, reactive surface area increases, and superficial velocity (and therefore mass transport) in the electrode decreases. The total DC electronic resistance of dry cells with no membrane was found to be less than 0.03 Ω cm^2, and therefore insignificant. Electrolyte solution conductivity for 0.6 M cerium and 5 M MSA is 306 mS cm^{-1}, so ionic conduction in the sub-millimeter thick electrode accounts for at most ~10% of the ASR observed in the discharge polarization data. These drawbacks of a thicker mesh stack are overcome by the beneficial addition of Pt surface area, as clearly seen in Figure 6b. Interspersing inactive Ti mesh (with similar geometry to the Pt mesh) between the Pt meshes does not impact performance, confirming that the addition of Pt area overwhelms the disadvantages of a thicker electrode. The comparison of Pt-Ti-Ti-Ti (Pt at flowfield) vs. Ti-Ti-Ti-Pt (Pt at membrane) illustrates that ionic-conduction path length between the active Pt site and the

membrane does not impact Pt-limited performance for low mesh number. Performance plateaus at 415 mW cm^{-2} at high mesh number as the thickness of the electrode, as well as membrane and (−) electrode, become significant limitations relative to the high-area (+) electrode. Increasing the flow rate (relative to the 4-mesh case) to maintain constant velocity (26 cm s^{-1}) in the electrode increases performance slightly (i.e. from 415 to 455 mW cm^{-2} for 8 meshes); mass transport is a small contribution to the limitation for the thick electrode in flow-through mode.

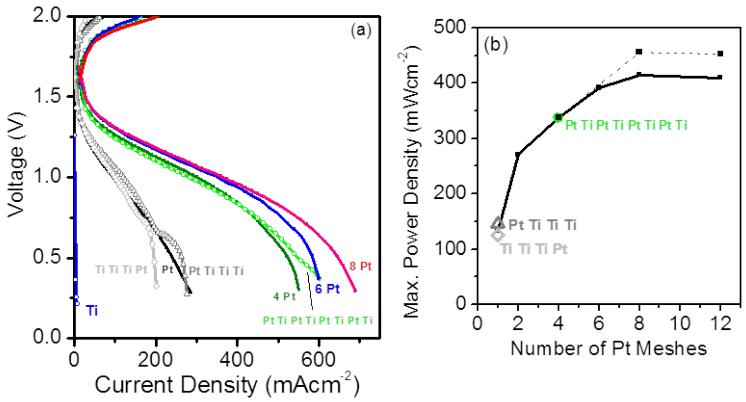

Figure 6. Impact of number of stacked meshes in the (+) electrode with 0.6 M Ce and 5 M MSA at 150 mL min^{-1}, and boiled NR212 membrane. Open symbols indicate cells in which Ti mesh was interspersed with the Pt mesh. (a) Charge and discharge polarization. (b) Peak discharge power density. Dashed line indicates flowrate was increased (300 mL min^{-1} for 8 meshes, 450 mL min^{-1} for 12 meshes) to achieve similar electrolyte velocity as for 4 meshes at 150 mL min^{-1}.

These results suggest cerium catalysis and mass transport both limit cell performance, consistent with the initial conclusions of previous work [15].

3.2.2 Hydrogen (−) electrode

Excellent performance of the hydrogen electrode in other redox flow cells leads us to expect that it does not limit performance in the present system [8,10]. To confirm this and optimize cell performance, various aspects of the hydrogen stream and (−) electrode were adjusted. The results are shown in the

Supplementary Information. Varying hydrogen back-pressure between 0 and 1.7 bar, and moisture content between 0 and 100% relative humidity at room temperature, had no impact on cell performance, showing that the liquid at the positive electrolyte keeps the membrane hydrated. The catalyst structure and platinum content of the (−) catalyst layer was varied between 4 mg cm^{-1} Pt-black or 0.4 mg cm^{-1} Pt-on-carbon, with little impact on performance. Deposition of the (−) catalyst layer on the membrane (catalyst-coated membrane, CCM) or on the microporous layer of the gas-diffusion layer (i.e., a gas-diffusion electrode, GDE) likewise did not affect performance. These results are in contrast to the H_2-Br_2 redox flow cell, for which cell performance is very sensitive to hydrogen and (−) electrode features, primarily due to adsorption of bromide ions on the Pt catalyst surface [8]. These results suggest cerium adsorption on the (−) catalyst is not a concern in the present system, and are consistent with the (+) cerium electrode limiting cell performance to such an extent that subtle changes in (−) electrode performance are not apparent.

3.2.3 Membrane

Pretreatment by boiling is known to increase significantly proton conductivity as well as transport of other species in redox flow cells [22,25]. The impact of pretreatment and thickness is shown for various Nafion membranes in Figure 7. The performance decreases slightly with membrane thickness, as expected from ionic resistance considerations. For example, current density at 1.3V is 138, 121, and 103 mA cm^{-2} for boiled 117, 212, and 211, respectively. Discharge performance is highly sensitive to boiling pretreatment (121 and 45 mA cm^{-2} at 1.3V for boiled and as-received 212, respectively). These results suggest interfacial resistance (at the electrolyte-membrane interface) dominates over bulk membrane conductivity, and is highly dependent on pretreatment. Based on these results, pre-boiling was chosen as standard for all other cells assembled in this work.

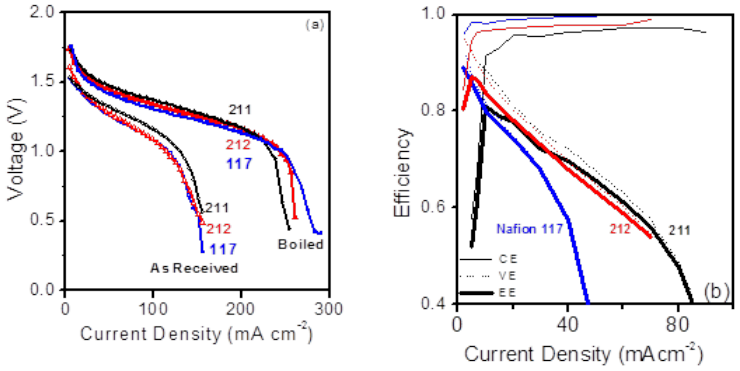

Figure 7. Effect of membrane thickness (N117, NR212, NR211) and pretreatment (as-received vs. boiled) on (a) discharge polarization and (b) efficiency (thin lines – coulombic efficiency, dashed lines – voltage efficiency, thick lines – energy efficiency). Stack of 4 Pt meshes as (+) electrode, 0.6 M Ce and 4 M MSA at 65 mL min^{-1}.

The impact of membrane thickness on efficiency, for pre-boiled membranes, is shown in Figure 7b. The maximum energy efficiency is limited by the coulombic efficiency, which is lower for thinner membranes and decreases rapidly at low current density (68, 96, and 98% coulombic efficiency at 7 mA cm^{-2} for 211, 212, and 117 respectively). This behavior is similar to that observed in other redox-flow systems where crossover of the aqueous active species causes self-discharge [22,31]. In those systems, transport of liquid through the membrane is observed. In both the H_2-Fe and H_2-Br_2 systems, liquid crossover is high enough that the liquid must be collected from the hydrogen exhaust and returned to the (+) side for continuous functioning of the device [10,22]. It is surprising, then, that no liquid was observed to cross through the membrane in the present H_2-Ce system, even after continuous cycling operation for several days with the hydrogen exhausted into a liquid trap. It is possible that contact with the cerium-MSA electrolyte solution dehydrates the membrane to such an extent that bulk liquid flux is prevented (moderate dehydration of the membrane in contact with HBr is observed) [32,33].

In the absence of bulk-liquid movement, we can envision Ce^{4+} diffusion through the membrane from (+) to (−) side, reduction to Ce^{3+} at the (−) side, and Ce^{3+} diffusion back to the (+) side as a mechanism for self-discharge, which is supported by the observed low coloumbic efficiency when a microporous separator showing high liquid crossover was used (see SI). Cerium is known to be highly mobile in Nafion membranes during PEM fuel-cell operation, and similar mobility should be expected here [34]. It is also possible that gas permeability of the membrane allows hydrogen to crossover to the (+) side where it could reduce Ce^{4+} at the Pt electrode. The self-discharge current required to produce the observed coulombic efficiency for N117 is calculated to be in the range 0.04 to 0.1 mA cm^{-2}, according to the equations developed in Ref [31]. This is similar to the 0.08 mA cm^{-2} equivalent flux predicted from the hydrogen permeability data for boiled N117 available in the literature .[35] Further detailed studies of the impact of cerium concentration and hydrogen pressure on the self-discharge rate are necessary to determine whether hydrogen or cerium crossover dominates. Regardless of the mechanism, it should be noted that the self-discharge current is extremely low, resulting in unusually high coulombic efficiency at low current density. For example, 99% coulombic efficiency is achieved for the present H_2-Ce system with boiled NR212 membrane (Figure 7b), whereas 65%, 86%, 90%, and 95-98% are achieved for the H_2-Br_2, H_2-Fe, Zn-Ce, and all-vanadium systems, respectively, at a similar current density [10,20,22,36,37].

A low-cost microporous separator was also tested (data shown in Supporting Information). Polarization performance was comparable to Nafion, however, a large amount of liquid crossover to the (−) electrode was observed. Bulk hydrogen gas transport to the (+) electrode was not observed. Very low coulombic efficiency occurred at low current density, consistent with reduction of crossover Ce^{4+} at the (−) electrode. This supports the thought that Ce^{4+} transport to the (−) electrode, if it occurs in Nafion membrane, results in self-discharge.

3.3 Electrolyte composition

Aqueous solutions of cerium methanesulfonate and MSA are the standard for cerium electrochemical half-cells, although there is no clear optimum for cerium or MSA concentration.[16] Cerium concentration affects reversibility [17], and solubility is known to depend on cerium oxidation state [38,39]. MSA concentration influences reversibility of the cerium reaction [17], the extent of oxygen evolution side reaction [17], cerium solubility [40,41], and solution conductivity and viscosity [17].

The impact of cerium concentration on performance was determined for solutions with 4 M MSA (see Supplementary Information). Solutions with 0.4 and 0.6 M Ce provide similar performance. The limiting discharge current for 0.2 M Ce is lower, consistent with concentration polarization. Solutions with 0.8 M and 1 M Ce were also tested, however, precipitation was observed during charging and the performance results were therefore not reliable or reproducible. To select between 0.4 M and 0.6 M Ce, efficiency was determined, and found to be nearly identical (comparable to the data for 1.9 V cutoff in Figure 3c). Therefore, 0.6 M Ce was chosen as the standard concentration, based on its higher volumetric energy density.

Following Reference [19], addition of 0.5 M HCl or H_2SO_4 to MSA was tested, but did not have a significant impact on cell performance. Complete replacement of MSA with H_2SO_4 was also evaluated, but cerium solubility and cell performance were both reduced. MSA concentration variation impacts performance minimally in the range 3-5 M, with 5 M providing the best performance (see Supplementary Information). Solutions with 2 M and 6 M MSA showed poor charging performance, and were not tested further.

3.4 Temperature dependence

Cell performance is expected to improve with operating temperature, as many properties are temperature-dependent, including transport properties, solution viscosity, and electrochemical kinetic parameters

[16,17]. Drawbacks to elevated temperature include the need for thermal insulation or preheating of the reactants, and reduced cerium solubility above 40 to 60°C (depending on solvent) [16,25]. Figure 8 shows that performance increases dramatically from room temperature to 60°C. Charge current of 373 mA cm^{-2}, discharge current of almost 1.5 A cm^{-2}, and peak discharge power density of 895 mW cm^{-2} are achieved at 60°C, whereas charge current of 199 mA cm^{-2}, discharge current of 660 mA cm^{-2}, and peak discharge power density of 410 mW cm^{-2} are achieved at room temperature. This greatly exceeds the performance of the present pre-optimized cell (Figure 4a, 225 mA cm^{-2} discharge current) and previously reported H_2-Ce system [15], as well as the H_2-Fe, [10], H_2-V [13], and other Ce-based redox flow cells including V-Ce [42], Pb-Ce [43], BH_4-Ce [44], and Zn-Ce [16]. The efficiency improvement provided by the combination of cell optimization of the preceding Sections and elevated temperature is also substantial, improving from 87% at 7 mA cm^{-2} for the baseline to 90% at 30 mA cm^{-2} for the improved cell. The coulombic efficiency is reduced slightly at elevated temperature, consistent with increased transport of crossover species, but the substantial increase in cell performance more than offsets this with an overall dramatic increase in energy efficiency. Peak energy efficiency of 90% is achieved at 30 mA cm^{-2}, but more importantly, the maximum current density at which an energy efficiency of 85% or greater is possible increased from 15 to 60 mA cm^{2}, although this is still below some of the other systems in terms of maximum current density at high efficiency. Peak discharge energy density of 21.4 Wh L^{-1} is achieved at 100 mA cm^{-2} and 50°C. This is similar to the conventional all-Vanadium system, and about half the energy density of advanced all-Vanadium and H_2-Br_2 systems [22,45].

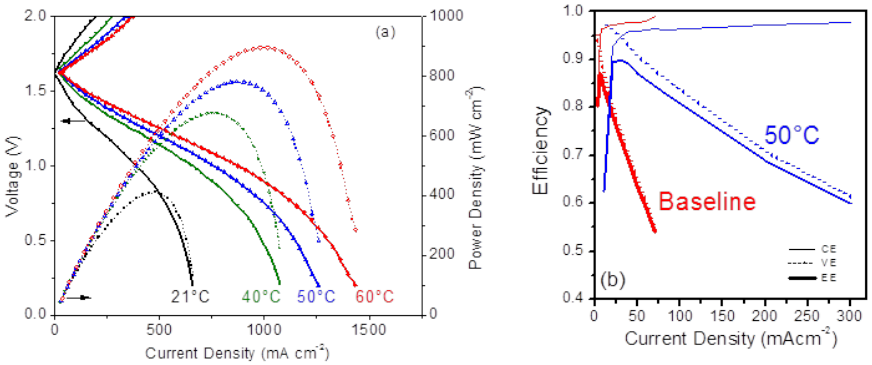

Figure 8. Impact of temperature on (a) polarization performance and (b) efficiency with a stack of 12 Pt meshes as (+) electrode, 0.6 M Ce and 5 M MSA at 150 mL min^{-1}, and boiled NR212 membrane. The room-temperature efficiency of the baseline cell is reproduced from Figure 3 for comparison.

4. Summary

The H_2-Ce redox flow cell was optimized using commercially-available cell materials and chemicals. Various aspects of the (+) and (-) electrodes including electrolyte solution, membrane, and cell operation were systematically varied, leading to a cell performance greatly exceeding previous reports. Cell performance was found to be sensitive to upper charge cutoff voltage, membrane boiling pretreatment, MSA concentration, (+) electrode surface area and flow pattern, and operating temperature. Performance was relatively insensitive to membrane thickness, Ce concentration, and all features of the (−) electrode and hydrogen flow. A maximum discharge power of 895 mW cm^{-2} was observed at 60°C. An energy efficiency of 90% was achieved at 50°C and 30 mA cm^{-2}.

A unique and surprising feature of this cell is the very low self-discharge (high coulombic efficiency), and absence of visible liquid transport through the membrane, accompanied by a relatively high membrane resistance. Further detailed study of the interaction between aqueous Ce-MSA and PEM membranes would be interesting. It would appear that identifying a membrane with higher conductivity, even at the expense of higher crossover, would be beneficial for energy-storage efficiency.

The high potential of the Ce reaction relative to the window of water stability means that high charging current (high overpotential) cannot be tolerated due to inefficiency associated with the oxygen evolution side reaction. In practice, therefore, asymmetric charge/discharge current density may be required. Substitution of a non-aqueous electrolyte may also alleviate this issue.

Suggestions for relevant future work include: determining impedance spectra under operating current; optimization of the (+) electrode architecture, particularly enhancing Pt surface area while minimizing Pt loading to reduce cost, perhaps *via* platiniziation of three-dimensional Ti structures designed to improve convective mass transport; discovery of improved electrocatalysts for the Ce reaction; detailed study of cerium, water, and MSA uptake and partitioning in the membrane and possible complexation in the electrolyte; identification of strategies including complexation to increase Ce solubility; durability and cycling assessment; and, system technoeconomic analysis.

Acknowledgements

The authors thank Philip Ross, Venkat Srinivasan, and Vincent Battaglia for helpful discussion. Samples of NSTF catalyst on Nafion membrane were prepared and supplied by Cemal Duru and Andy Steinbach (3M Company). This work was funded by the U.S. Department of Energy under contract no. DE-AC02-05CH11231.

References

[1] A.Z. Weber, M.M. Mench, J.P. Meyers, P.N. Ross, J.T. Gostick, Q. Liu, J. Appl. Electrochem. 41 (2011), 1137-1164.

[2] M.L. Perry, A.Z. Weber, J. Electrochem. Soc. 163 (2016) A5064-A5067.

[3] J. Noack, N. Roznyatovskaya, T. Herr, P. Fischer, Angew. Chem. Int. Ed. 54 (2015) 2–36.

[4] M. Skyllas-Kazacos, M.H. Chakrabarti, S.A. Hajimolanab F.S. Mjalli, M. Saleem. J. Electrochem. Soc. 158 (2011) R55-R79.

[5] G.L. Soloveichik, Chem. Rev. 115 (2015) 11533–11558.

[6] Y.V. Tolmachev, Russian J. Electrochem. 50 (2014) 301–316.

[7] K.T. Cho, M.C. Tucker, A.Z. Weber, Energy Technol., accepted.

[8] M.C. Tucker, K.T. Cho, A.Z. Weber, G. Lin, T.V. Nguyen, J. Appl. Electrochem. 45 (2015) 11-19.

[9] K.T. Cho, P. Albertus, V. Battaglia, A. Kojic, V. Srinivasan, A.Z. Weber, Energy Technol. 1 (2013) 596-608.

[10] M.C. Tucker, K. T. Cho, A.Z. Weber, J. Power Sources 245 (2014) 691-697.

[11] M.C. Tucker, V. Srinivasan, P.N. Ross, A.Z. Weber, J. Appl. Electrochem. 43 (2013) 637-644.

[12] V. Watson, D. Nguyen, E.E. Effiong, E.E. Kalu, ECS Electrochem. Lett. 4 (2015) A72-A75.

[13] V. Yufit, B. Hale, M. Matian, P. Mazur, N.P. Brandon, J. Electrochem. Soc. 160 (2013) A856-A861.

[14] H. Hewa Dewage, V. Yufit, N.P. Brandon, J. Electrochem. Soc. 163 (2016) A5236-A5243.

[15] H. Hewa Dewage, B. Wu, A. Tsoi, V. Yufit, G. Offer, N.P. Brandon, J. Mater. Chem. A 3 (2015) 9446-9450.

[16] F.C. Walsh, C. Ponce de León, L. Berlouis, G. Nikiforidis, L.F. Arenas-Martinez, D. Hodgson, D. Hall, ChemPlusChem 80 (2015) 288 – 311.

[17] P.K. Leung, C. Ponce de León, C.T.J. Low, F.C. Walsh, Electrochimica Acta 56 (2011) 2145–2153.

[18] Z. Xie, Q. Liu, Z. Chang, X. Zhang, Electrochimica Acta 90 (2013) 695– 704.

[19] G. Nikiforidi, W.A. Daoud, Electrochimica Acta 141 (2014) 255-262.

[20] G. Nikiforidis, L. Berlouis, D. Hall, D. Hodgson, J. Power Sources 243 (2013) 691– 698.

[21] K.T. Cho, M.C. Tucker, M. Ding, P. Ridgway, V.S. Battaglia, V. Srinivasan, A.Z. Weber, ChemPlusChem 80 (2015) 402-411.

[22] M.C. Tucker, K.T. Cho, F.B. Spingle, A.Z. Weber, G. Lin, J. Power Sources 284 (2015) 212-221.

[23] D.S. Aaron, Q. Liu, Z. Tang, G.M. Grim, A.B. Papandrew, A. Turhan, T.A. Zawodzinski, M.M. Mench, J.Power Sources 206 (2012) 450–453.

[24] K.T. Cho, P. Ridgway, A.Z. Weber, S. Haussener, V. Battaglia, V. Srinivasan, J. Electrochem. Soc., 159 (2012) A1806-A1815.

[25] W. Xie, R.M. Darling, M.L. Perry, J. Electrochem. Soc., 163 (2016) A5084-A5089.

[26] M.K. Debe, Nature 486 (2012) 43–51.

[27] V. Devadoss, C.A. Basha, K. Jayaraman, J. Ind. Eng. Chem. Res. 47 (2008) 4607–4616.

[28] A.A. Shah, M.J. Watt-Smith, F.C. Walsh, Electrochimica Acta 53 (2008) 8087–8100.

[29] B. Huskinson, M.J. Aziz, Energy Sci. Technol., 5 (2013) 1-16.

[30] P. Ridgway, K. Cho, V.S. Battaglia, A.Z. Weber, V. Srinivasan Redox kinetics of the bromine-bromide reaction for flow batteries, Presented at the 220th meeting of the Electrochemical Society, Boston, MA (2011).

[31] R.M. Darling, A.Z. Weber, M.C. Tucker, M.L. Perry, J. Electrochem. Soc., 163 (2016) A5014-A5022.

[32] R.S. Yeo, D.T. Chin, J. Electrochem. Soc. 127 (1980) 549-555.

[33] A. Kusoglu, K.T. Cho, R.A. Prato, A.Z. Weber, Solid State Ionics 252 (2013) 68-74.

[34] S.M. Stewart, D. Spernjak, R. Borup, A. Datye, F. Garzon, ECS Electrochem. Lett. 3 (2014) F19-F22.

[35] K. Broka, P. Ekdunge, J. Appl. Electrochem. 27 (1997) 117-123.

[36] A. Benjamin, E. Agar, C.R. Dennison, E.C. Kumbur, Electrochem. Comm. 35 (2013) 42–44.

[37] S. Kim, E. Thomsen, G. Xia, Z. Nie, J. Bao, K. Recknagle, W. Wang, V. Viswanathan, Q. Luo, X. Wei, A. Crawford, G. Coffey, G. Maupin, V. Sprenkle, J. Power Sources 237 (2013) 300–309.

[38] T. Raju, C.A. Basha, J. Portugaliae Electrochim. Acta 23 (2005) 367-378.

[39] T. Raju, C.A. Basha, J. Ind. Eng. Chem. Res. 47 (2008) 8947-8952.

[40] R.M. Spotnitz, R. P. Kreh, J.T. Lundquist, P.J. Press, J. Appl. Electrochem. 20 (1990) 209 –215.

[41] R.P. Kreh, R.M. Spotnitz, J.T. Lundquist, J. Org. Chem. 54 (1989) 1526-1531.

[42] M. Govindan, K. He, I.-S. Moon, Int. J. Electrochem. Sci., 8 (2013) 10265-10279.

[43] Z. Na, S. Xu, D. Yin, L. Wang, J. Power Sources 295 (2015) 28-32.

[44] N. Da Mota, D.A. Finkelstein, J.D. Kirtland, C.A. Rodriguez, A.D. Stroock, H.D. Abruña, J. Am. Chem. Soc. 134 (2012) 6076-6079.

[45] L. Li, S. Kim, W. Wang, M. Vijayakumar, Z. Nie, B. Chen, J. Zhang, G. Xia, J. Hu, G. Graff, J. Liu, Z. Yang, Adv. Energy Mater. 1 (2011) 394–400.

Figure Captions

Figure 1. Schematic of H_2-Ce redox flow cell.

Figure 2. Performance variation with state of charge. (a) Open-circuit voltage and (b) charge and discharge polarization for a stack of 4 Pt meshes as (+) electrode, 0.6 M Ce and 4 M MSA at 65 mL min^{-1}, and boiled NR212 membrane. (c) AC impedance at 120 mA cm^{-2} discharge current for a stack of 8 Pt meshes as (+) electrode, 0.6 M Ce and 5 M MSA at 65 mL min^{-1}, and boiled NR212 membrane.

Figure 3. (a) Full charge/discharge cycle at 10 mA cm^{-2} with 1.9 V charge cut-off. Impact of charge cut-off voltage on (b) Ce utilization and (c) efficiency (thin lines – coulombic efficiency, dashed lines – voltage efficiency, thick lines – energy efficiency). Stack of 4 Pt meshes as (+) electrode, 0.6 M Ce and 4 M MSA at 65 mL min^{-1}, and boiled NR212 membrane.

Figure 4. Impact of (+) type on performance. (a) Single woven Pt, expanded platinized Nb, or expanded platinized Ti mesh as (+) electrode, 0.6 M Ce and 4 M MSA at 65 mL min^{-1}, and boiled NR212 membrane. (b) Enhancement of cell performance with addition of NSTF Pt layer on the (+) side of the membrane. Single Pt mesh (with or without NSTF) as (+) electrode, 0.6 M Ce and 5 M MSA at 70 mL min^{-1}, and boiled NR212 membrane.

Figure 5. Influence of flowrate on discharge performance. Stack of 4 Pt meshes as (+) flowthrough electrode, 0.6 M Ce and 4 M MSA, and boiled NR212 membrane.

Figure 6. Impact of number of stacked meshes in the (+) electrode with 0.6 M Ce and 5 M MSA at 150 mL min^{-1}, and boiled NR212 membrane. Open symbols indicate cells in which Ti mesh was interspersed with the Pt mesh. (a) Charge and discharge polarization. (b) Peak discharge power density. Dashed line

indicates flowrate was increased (300 mL min^{-1} for 8 meshes, 450 mL min^{-1} for 12 meshes) to achieve similar electrolyte velocity as for 4 meshes at 150 mL min^{-1}.

Figure 7. Effect of membrane thickness (N117, NR212, NR211) and pretreatment (as-received vs. boiled) on (a) discharge polarization and (b) efficiency (thin lines – coulombic efficiency, dashed lines – voltage efficiency, thick lines – energy efficiency). Stack of 4 Pt meshes as (+) electrode, 0.6 M Ce and 4 M MSA at 65 mL min^{-1}.

Figure 8. Impact of temperature on (a) polarization performance and (b) efficiency with a stack of 12 Pt meshes as (+) electrode, 0.6 M Ce and 5 M MSA at 150 mL min^{-1}, and boiled NR212 membrane. The room-temperature efficiency of the baseline cell is reproduced from Figure 3 for comparison.